

Annual Review of Condensed Matter Physics

Majorana Zero Modes in Networks of Cooper-Pair Boxes: Topologically Ordered States and Topological Quantum Computation

Yuval Oreg¹ and Felix von Oppen²

¹Department of Condensed Matter Physics, Weizmann Institute of Science, Rehovot, 76100 Israel; email: yuval.oreg@weizmann.ac.il

²Dahlem Center for Complex Quantum Systems and Fachbereich Physik, Freie Universität Berlin, 14195 Berlin, Germany

Annu. Rev. Condens. Matter Phys. 2020. 11:397–420

First published as a Review in Advance on December 3, 2019

The *Annual Review of Condensed Matter Physics* is online at conmatphys.annualreviews.org

<https://doi.org/10.1146/annurev-conmatphys-031218-013618>

Copyright © 2020 by Annual Reviews.
All rights reserved

Keywords

topological superconductivity, topological states of matter

Abstract

Recent experimental progress introduced devices that can combine topological superconductivity with Coulomb-blockade effects. Experiments with these devices have already provided additional evidence for Majorana zero modes in proximity-coupled semiconductor wires. They also stimulated numerous ideas for how to exploit interactions between Majorana zero modes generated by Coulomb charging effects in networks of Majorana wires. Coulomb effects promise to become a powerful tool in the quest for a topological quantum computer as well as for driving topological superconductors into topologically ordered insulating states. Here, we present a focused review of these recent developments, including discussions of recent experiments, designs of topological qubits, Majorana-based implementations of universal quantum computation, and topological quantum error correction. Motivated by the analogy between a qubit and a spin-1/2 degree of freedom, we also review how coupling between Cooper-pair boxes leads to emergent topologically ordered insulating phases.

ANNUAL
REVIEWS **CONNECT**

www.annualreviews.org

- Download figures
- Navigate cited references
- Keyword search
- Explore related articles
- Share via email or social media

1. INTRODUCTION

Isolated Majorana zero modes in topological superconductors are associated with a degeneracy of the ground state. Up to corrections that are exponential in the distance between the Majoranas, every two Majoranas induce a twofold degeneracy. Remarkably, no local measurement can reveal the specific state that a system assumes within the ground-state manifold. This implies that quantum information stored within this manifold is strongly protected against local sources of decoherence (1).

For the same reason, manipulation of this quantum information necessarily requires nonlocal operations. An important class of such nonlocal operations are braiding processes exploiting the nonabelian statistics of the Majorana zero modes (1–5). Adiabatic braiding of Majoranas leaves the system within the ground-state manifold, but generally not in the same state. Instead, braiding is associated with a unitary evolution within the ground-state manifold, and this unitary evolution can be exploited for quantum information processing (1).

In this review, we focus on charging effects in Majorana systems. As the charging energy is a global property of the system, it is a second important source of nonlocality. A quantum wire in a topological superconducting phase has two Majorana bound states, one at each end, and a twofold degenerate ground state (6). One ground state is a fully paired state. A second ground state accommodates an unpaired fermion by virtue of the zero-energy fermionic excitation which can be formed from the two Majorana zero mode operators. Thus, the two ground states are distinguished by their fermion number parity, with one state having even and the other having odd fermion number parity. Charging effects are sensitive to the global number of electrons in a sample. They can consequently distinguish between, and lift the degeneracy of, the even and odd fermion-parity ground states (7).

Recent theoretical and experimental progress shows that charging effects constitute a powerful tool in Majorana devices. They can be used to probe Majorana physics, to bootstrap these systems for realizing correlated and topologically ordered phases, and to construct a topological quantum computer. The building blocks underlying these developments are Coulomb-blockaded islands with an even number of Majorana zero modes, based on quantum wires with strong spin-orbit coupling and proximity-induced superconductivity (8, 9).

A representative example is the Majorana box qubit or tetron (10, 11), which contains four Majorana zero modes on the same superconducting island. Charging fixes the overall electron number, and hence the overall fermion parity, thereby reducing the fourfold ground-state degeneracy associated with the four Majorana zero modes to a twofold degeneracy. Similarly, hexons are based on six Majorana zero modes and have a fourfold ground-state degeneracy.

In the context of quantum computation, tetrons and hexons can be viewed as topological qubits (10, 11). In addition to their topological protection against local sources of decoherence, the charging energy protects these qubits against quasiparticle poisoning processes that change the tetron's fermion parity and thereby take it out of its computational subspace. Topological qubits based on Coulomb-blockaded Majorana systems are reviewed in Section 3, and current ideas on how they can be used for topological quantum computation are discussed in Section 4.

Assemblies of Cooper-pair boxes can also be viewed as a practical means of introducing Coulomb interactions into networks of hybridized Majorana zero modes. In the absence of Coulomb interactions, such a network may form two-dimensional topological superconducting states. Adding strong Coulomb interactions induces a superconductor-to-insulator transition. Remarkably, the resulting insulating phases may be nontrivial topologically ordered states.

This can be understood most directly by viewing tetrons and hexons as implementations of local spin-1/2 degrees of freedom (12). Their assembly into coupled networks can then be used to implement various Hamiltonians with topologically ordered ground states. Effective Zeeman

fields and spin interactions are realized by hybridizing Majoranas within or between Coulomb islands. Remarkably, this not only results in Zeeman or exchange couplings but also naturally generates spin-cluster interactions involving more than two spins. In addition to spin models, such networks can also directly implement field-theoretical Hamiltonians and parton constructions (13–15). These developments are reviewed in Section 5.

Closely related constructions also play an important role in the context of quantum computing. Although dephasing times of topological qubits may be long, they remain finite, and large-scale quantum computations that run longer than the dephasing time require quantum error correction. Topological quantum error correction (16) relies on encoding quantum information in degenerate ground states of topologically ordered phases similar to those reviewed in Section 5. However, instead of implementing their Hamiltonian, active quantum error correction is based on measurement-based feedback protocols that stabilize the quantum information within these ground-state manifolds. In Section 6, we review how to combine topological qubits with topological quantum error correction on the basis of bosonic surface or color codes as well as closely related Majorana fermion codes.

Even when quantum error correction turns out to be necessary, the use of topological qubits remains advantageous over other qubit types as long as their topological protection results in superior decoherence times. If this is the case, a smaller number of physical qubits is required to realize a single logical qubit with a specified error resilience. The use of topological qubits may then considerably reduce the required hardware overhead.

The study of Coulomb-blockaded Majorana systems owes much to seminal experimental work. The sample quality of proximity-coupled semiconductor wires was much improved by realizing that the superconductor can be grown epitaxially on the semiconductor quantum wire (17). Unlike earlier experiments, epitaxial wires exhibit a hard induced superconducting gap, a precondition for any application of Majorana systems as effective spin-1/2 degrees of freedom or topological qubits. Importantly, the epitaxial Al layer typically has a small thickness so that the overall dimensions of the system are sufficiently small for charging effects to be important (18). The current status of experiment is briefly discussed in Section 2.

This is a focused review and there are many subjects that are outside its scope. Although our review addresses interactions in Majorana systems, we explicitly focus on charging physics. We are not concerned with the interaction physics of individual Majorana wires but rather with how charging effects can be exploited for engineering topologically ordered states or a topological quantum computer. There have been numerous studies of the effects of microscopic interactions in individual wires, e.g., studying the phase diagram of interacting Kitaev wires (19) or the effect of interactions on the phase diagram of proximity-coupled semiconductor quantum wires (20–22). These works are outside the scope of the present review. This review also does not cover the Majorana–Kondo effect (23), which is predicted to occur when a single Coulomb-blockaded box with Majorana bound states is coupled to metallic leads. For recent reviews of other aspects of Majorana zero modes, we refer the interested reader to References 24–30.

2. MAJORANA ZERO MODES AND COULOMB BLOCKADE IN QUANTUM WIRES

2.1. Majorana Cooper-Pair Box

A Cooper-pair box is a floating superconducting sample with a fixed number of electrons n that is controlled through a gate voltage V_g applied to a gate capacitor C_g . For a nontopological superconductor, the ground-state energy exhibits an even–odd effect as a function of n . Ground states with an unpaired electron have an energy that is larger by the pairing energy Δ , relative to a fully

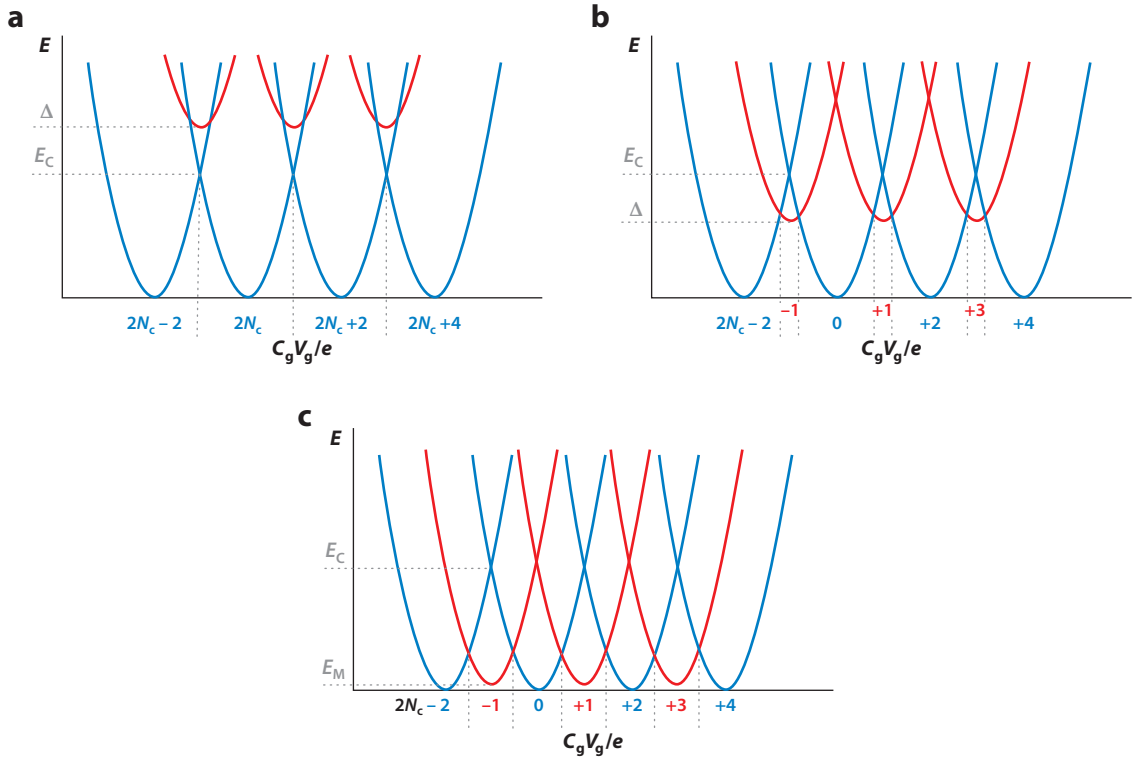


Figure 1

Ground state energy as a function of gate voltage V_g for nontopological superconductors with (a) $\Delta > E_C$ and (b) $\Delta < E_C$, as well as for (c) a topological superconductor with Majorana zero modes (that have a small matrix element, E_M , between them). Here, $N_c = \langle \hat{N}_c \rangle$ is the number of Cooper pairs.

paired state. Thus, the ground-state energy equals $E = E_C(n - C_g V_g / e)^2$ for fully paired states and $E = E_C(n - C_g V_g / e)^2 + \Delta$ for states with an unpaired electron. Here, $E_C = e^2 / 2C$ denotes the charging energy of the island.

As illustrated in **Figure 1**, the number of electrons in the ground state depends on the gate voltage. The electron number changes whenever two charge states become degenerate. For $\Delta > E_C$, the degeneracies are between states that differ by two electrons and electrons are added in pairs. For $\Delta < E_C$, the degeneracies are between states that differ by one electron and electrons are added one by one. The Coulomb-blockade peaks, which are equidistant in gate voltage for $\Delta > E_C$, split in two for $\Delta < E_C$.

If the island is a topological superconductor, unpaired electrons can be accommodated by midgap states associated with the Majorana zero modes. Retaining the residual overlap between the Majoranas, these states are associated with an (exponentially small) single-particle energy E_M . Thus, the charging Hamiltonian can be written as

$$H_{\text{charging}} = E_C (\hat{n} - C_g V_g / e)^2 + E_M \hat{n}_M. \quad 1.$$

The electron number operator $\hat{n} = 2\hat{N}_c + \hat{n}_M$ involves the Cooper-pair number operator \hat{N}_c and the fermionic occupation \hat{n}_M of the Majorana zero modes. For two Majoranas γ_1 and γ_2 , \hat{n}_M can be related to the fermion parity operator as $\hat{n} = (1 - i\gamma_1 \gamma_2) / 2$. As long as $E_C > E_M$, variations in the

gate voltage add electrons in steps of one. The Coulomb-blockade peaks again become equidistant for isolated Majorana zero modes with $E_M = 0$ (albeit with half the distance in V_g compared to the nontopological regime with $\Delta > E_C$). Notice that for more than two Majoranas, the charging energy only distinguishes states with different fermion parities as even occupations of the midgap states can be compensated by the number of Cooper pairs.

Josephson coupling the island to a bulk nontopological superconductor through a Josephson junction provides additional control on the charging energy by effectively interpolating between a floating ($E_C \gg E_J$) and a grounded ($E_J \gg E_C$) superconducting island (31, 32). The Josephson coupling of strength E_J adds $H_J = E_J \cos \hat{\phi}$ to the charging Hamiltonian, where the superconducting phase difference $\hat{\phi}$ is canonically conjugate to the Cooper-pair number, $[\hat{N}_c, \hat{\phi}] = i$. In particular, the Josephson coupling hybridizes states that differ by pairs of electrons and thereby lifts the degeneracies in **Figure 1** between charge states that differ by an even number of electrons.

2.2. Experiments

Early experiments (33–36) on Majorana zero modes in quantum wires largely focused on zero-bias anomalies in the tunneling conductance. More recently, this type of experiment showed evidence for the predicted (37, 38) conductance quantization (39, 40) and was extended to full-shell wires (41, 42), planar Josephson junctions (43–45), and chains of magnetic adatoms on superconducting substrates (46–50).

Coulomb-blockade effects provide alternative signatures of Majorana zero modes in semiconductor quantum wires (18). These experiments were in part enabled by the recent experimental development of semiconductor quantum wires with epitaxial superconductor (17) as well as related work on two-dimensional electron systems with epitaxial superconductor (51). Due to the atomically clean interface, the superconductor (Al) induces a hard proximity gap in the quantum wire (InAs) (52). The induced gap is comparable with the Al gap, even when the thickness of the Al layer is much smaller than the superconducting coherence length. This is a result of strong coupling between semiconductor and superconductor in conjunction with disorder in the superconductor, for instance, due to diffusive reflections from its exposed surface (53–56).

Proximity-coupled semiconductor quantum wires can be tuned into the topological superconducting phase by increasing the applied magnetic field (8, 9). Assuming that $\Delta > E_C$ at zero magnetic field, we then expect a doubling of the number of Coulomb-blockade peaks as a Coulomb-blockaded wire is tuned across the topological phase transition. This doubling was indeed observed in the experiment reported in Reference 18. The small deviations from perfectly equidistant Coulomb-blockade peaks could be used to extract the residual Majorana hybridization E_M . We note that the experiment presumably showed an additional intermediate regime in which the magnetic field suppresses Δ below E_C before the wire becomes topological. This regime exhibits split but not yet equidistant Coulomb-blockade peaks owing to single-electron additions. As analyzed in Reference 57, current through the Coulomb-blockaded wire segment is carried by electron pair transfer, single-electron transfer, or electron teleportation (7), depending on the magnetic-field regime.

Majorana teleportation refers to coherent single-electron transport in the Coulomb-blockade regime, enabled by spatially separated Majorana zero modes (7). More generally, coherence is an essential ingredient in protocols to use Majoranas for quantum computation applications (see Sections 3, 4, and 6 below). A minimal test of coherence is provided by measurements of the transmission phase through a Coulomb-blockaded Majorana wire by embedding it in one arm of an Aharonov–Bohm interferometer. Detailed theoretical predictions were presented in Reference 58. A recent experiment (59) exhibits coherent Aharonov–Bohm oscillations and a phase

shift of π when the number of electrons of the island is increased by one. A detailed analysis of the experiment suggests that for short wires, transport does not entirely proceed through the Majorana zero modes. Coulomb-blockade physics has also been used for probing quasiparticle poisoning processes in hybrid semiconductor–superconductor systems (60).

3. TETRONS AND HEXONS AS BASIC BUILDING BLOCKS

3.1. Tetrons

Even though a single quantum wire in a topological superconducting phase has two degenerate ground states, its ground-state manifold does not provide a local spin or qubit degree of freedom. This is because its two ground states differ in fermion parity. Due to fermion parity superselection, it is impossible to prepare an isolated system in a coherent superposition of such states (61).

A local spin or qubit degree of freedom can only be realized using (at least) two quantum wires with four Majoranas, $\gamma_1, \gamma_2, \gamma_3,$ and γ_4 (see **Figure 2**; 10–12). The resulting ground-state manifold is four dimensional, with two states having even and two states having odd fermion parity. If we denote the even and the odd fermion parity ground states of the individual wires by $|e\rangle$ and $|o\rangle$, respectively, the four ground states can be chosen as $|ee\rangle, |eo\rangle, |oe\rangle,$ and $|oo\rangle$, where the two entries denote the fermion parities $i\gamma_1\gamma_2$ and $i\gamma_3\gamma_4$ of the wires. We can now encode the qubit—or equivalently, the spin degree of freedom—in the subspace with overall even fermion parity and use the computational basis

$$|0\rangle = |ee\rangle \quad 2.$$

$$|1\rangle = |oo\rangle. \quad 3.$$

The qubit subspace is then defined by the fermion-parity constraint,

$$P = (i\gamma_1\gamma_2)(i\gamma_3\gamma_4) = 1. \quad 4.$$

This is known as a Majorana box qubit or tetron (10, 11).

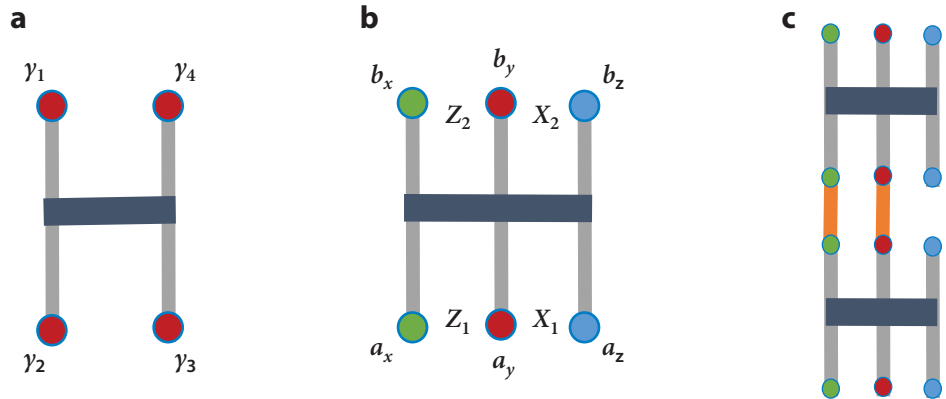


Figure 2

(a) Tetron with four Majorana zero modes (red) on two quantum wires (gray) connected by a conventional superconducting bridge (blue). Tetrons can be viewed as qubits or local spin-1/2 degrees of freedom. (b) Hexon with six Majoranas (green, red, and blue circles) encoding two spin-1/2 degrees of freedom. (c) Setup for measuring $Z_i \otimes Z_j$ of two qubits. Conventional semiconductors (orange) induce tunnel couplings between the Majoranas in Z_i and Z_j . The procedure generalizes to arbitrary Pauli products.

It is useful to express the Pauli spin operators in the qubit subspace in terms of the Majorana operators. We choose the computational basis states as eigenstates of the Pauli-Z operator,

$$Z = i\gamma_1\gamma_2 = i\gamma_3\gamma_4. \quad 5.$$

Here, the second equality follows from the parity constraint in Equation 4. The Pauli-X operator can then be chosen as

$$X = i\gamma_2\gamma_3 = i\gamma_1\gamma_4, \quad 6.$$

and the Pauli-Y operator,

$$Y = i\gamma_1\gamma_3 = -i\gamma_2\gamma_4, \quad 7.$$

follows from the identity $Y = iXZ$. The anticommutation relations $\{\gamma_\alpha, \gamma_\beta\} = 2\delta_{\alpha\beta}$ for the Majorana operators imply that these Pauli operators satisfy the Pauli algebra. In particular, the operators square to unity, and different Pauli operators anticommute.

Processes that add or remove an electron (or more generally an odd number of electrons) from a tetron change its fermion parity and cause leakage errors of the qubit. Charging physics can be used to suppress these quasiparticle poisoning processes (10, 11). If the two quantum wires are proximity-coupled to the same floating superconducting island with nonzero charging energy, the ground state has a fixed overall number of electrons and, hence, overall fermion parity due to the island's charging energy. At temperatures well below the charging energy, processes that change the electron number require thermal activation and are exponentially suppressed. In devices with epitaxial superconductors, this can be achieved by a sufficiently strong link between the two Majorana wires made from a nontopological superconductor (see **Figure 2**).

The topological nature of a tetron qubit becomes most pronounced for long wires for which the distance L between the Majoranas is large compared to the coherence length ξ of the topological superconductor, and the residual Majorana splitting $\sim e^{-L/\xi}$ becomes exponentially small. At the same time, poisoning processes are suppressed as $e^{-E_C/T}$ due to the charging energy E_C (T denotes the temperature). Because the charging energy scales (approximately inversely proportional) with the length of the wires, this suppression is more pronounced in short wires. This competition implies that there is an optimal length of the Majorana wires making up the tetron, which is determined by $E_C/T \sim L/\xi$ (11).

3.2. Hexons

Tetrons encode a single qubit or spin degree of freedom within a subspace defined by four Majoranas. It is clear from the ground-state degeneracy of a system with N Majoranas that, in principle, fewer Majoranas suffice to encode a qubit.

A hexon (10, 11) is a device that encodes two qubits using six Majoranas on three Majorana wires, thus effectively using three Majoranas per qubit. The basic design of a hexon is shown in **Figure 2**. Based on the twofold degenerate ground states of each of the three wires, the ground-state manifold of the hexon is eightfold degenerate in the absence of charging effects. The manifold separates into two sets of four states that differ in their fermion parity. If the wires are again linked by nontopological superconductors, the charging energy of the overall structure splits the energy of the even and odd fermion parity subspaces, and we encode the two qubits or spins, say, in the even fermion parity subspace.

Instead of writing down the explicit computational basis states, it is more concise to express the Pauli operators for the two qubits (labeled a and b) in terms of the Majorana operators. We can

encode the first qubit using the lower three Majoranas $a_x, a_y,$ and $a_z,$ and define the Pauli operators through $Z_a = ia_x a_y,$ and $X_a = ia_y a_z,$ which also implies that $Y_a = ia_x a_z.$ The second qubit can then be encoded in the same manner using the upper three Majoranas $b_x, b_y,$ and $b_z.$ The corresponding Pauli operators are illustrated in **Figure 2.** As for the tetron, these operators satisfy the Pauli algebra for each qubit. Furthermore, Pauli operators associated with different qubits commute.

Within hexons, the two-qubit parity operators are simple Majorana hybridizations. Consider the operator $ia_x b_x$ involving the Majoranas of the leftmost wire. As different Majorana operators anticommute, this operator anticommutes with the Pauli-Z and Pauli-Y operators of both encoded qubits, but commutes with the Pauli-X operators. We can thus identify

$$X_a \otimes X_b = ia_x b_x. \quad 8.$$

Similar considerations imply that

$$Z_a \otimes Z_b = ia_z b_z \quad 9.$$

involving the hybridization of the two Majoranas of the rightmost wire, and

$$Y_a \otimes Y_b = ia_y b_y \quad 10.$$

involving the hybridization of the two Majoranas of the central wire. Formally, these relations reflect the fermion parity constraint

$$\mathcal{P} = ia_x a_y a_z b_x b_y b_z = 1 \quad 11.$$

of the hexon.

3.3. Qubit Initialization and Readout

Charging physics can be exploited to read out tetron and hexon qubits (10, 11). Readout is particularly flexible for hexon-based qubits, and we focus on this case below.

To read out the Pauli-Z operator of the lower qubit of the hexon in **Figure 2,** one may tunnel couple a quantum dot to the ends of the wires hosting Majoranas a_x and $a_y.$ Both the tunnel junctions and the quantum dot can, for instance, be defined by plunger gates in additional semiconductor wires without epitaxial superconductor. Assuming that the quantum dot has one relevant energy level in the vicinity of the Fermi energy, the energy of this level will be shifted by the coupling to the hexon and the resulting shift depends in general on $Z_a = ia_x a_y.$ Thus, the energy shift can be used to measure $Z_a.$

To understand this, we consider the energy shift $\Delta\epsilon$ of the dot level in second-order perturbation theory. Assuming that the quantum dot level is occupied, the basic process changing its energy involves an electron tunneling into the hexon and back. The virtual intermediate state is an excited charge state so that it has a nonzero energy denominator $\Delta E.$ Within the low-energy subspace, the tunnel coupling takes the form

$$H_T = d^\dagger (t_x a_x + t_y a_y) + \text{h.c.}, \quad 12.$$

where d^\dagger adds an electron to the quantum dot level. We then find for the energy shift

$$\begin{aligned} \Delta\epsilon &= \frac{1}{\Delta E} \{ |t_x|^2 a_x^2 + |t_y|^2 a_y^2 + t_x^* t_y a_x a_y + t_y^* t_x a_y a_x \} \\ &= \frac{1}{\Delta E} \{ |t_x|^2 + |t_y|^2 + 2\text{Im}(t_x^* t_y) Z_a \}, \end{aligned} \quad 13.$$

which depends explicitly on the Pauli- Z operator Z_a of the lower hexon qubit. Although the two tunnel contacts to the hexon can be closely spaced in real space, this is not a local measurement as the two contacts are effectively at two far ends of the system.

Several ways have been proposed to measure the energy shift of the quantum dot (11). An alternative readout scheme is based on conductance measurements (10). In this interference measurement, the amplitude for a current path through the hexon passing both a_x and a_y depends on Z_a . This can be read out by measuring the interference contribution to the conductance with an additional reference arm.

An interesting feature of these measurement schemes is that they read out the qubit strictly along the z axis if overlaps between the Majoranas can be neglected within the hexon. Deviations from the z axis would necessarily involve Majoranas other than a_x and a_y , whose contributions are exponentially suppressed for the same reason that makes the ground-state degeneracy exponentially precise. As long as these measurements are projective, they can also be used for qubit initialization. Furthermore, such projective measurements are also a prerequisite for the implementation of several quantum gate operations described further below.

Another very useful aspect of these proposed measurement schemes is that they can be implemented for all three Pauli bases with equal ease and equal precision. Measuring the Pauli operators X_a or Y_a instead of Z_a simply requires contacts to different pairs of Majorana operators. For hexons, all these Majoranas are in close proximity in real space. Similar schemes have been proposed for tetrons (10, 11), but they require additional topological quantum wires that act as coherent links.

3.4. Braiding Protocols in Coulomb-Blockaded Majorana Systems

Their nonabelian statistics is a coveted property of Majorana zero modes. Braiding Majoranas γ_i and γ_j implements the unitary transformation $B_{ij} = \exp\{\pi\gamma_i\gamma_j/4\}$ in the ground-state manifold (3–5, 24, 28, 62, 63). Charging physics can be helpful in designing corresponding experimental tests. The most immediate test of braiding in semiconductor quantum wires relies on explicitly moving Majorana zero modes in a T-junction structure (62). Alternatively, in a closely related procedure, braiding can be implemented by judicious hybridization protocols of Majorana zero modes (28, 64). Coulomb charging provides a possible means of implementing this coupling. A Coulomb-assisted braiding scheme was discussed in Reference 31. This scheme exploits that the charging effects can be tuned with exponential accuracy by adjusting magnetic fluxes in Josephson junctions. A purely electric scheme for Coulomb-assisted braiding in a T-junction was proposed in Reference 32.

A closely related but potentially simpler experiment exploits the possibility of measuring a hexon in the Pauli X , Y , and Z bases (65). After initializing the qubit by a measurement in the $Z = ia_x a_y$ basis, measuring in the $Y = ia_x a_z$ basis will give both measurement outcomes with equal probability. Because $B_{23}^\dagger Z B_{23} = Y$, this is essentially equivalent to an experiment in which one measures a second time in the Z basis after braiding a_y and a_z , which also yields both measurement outcomes with equal probability.

4. MAJORANA-BASED TOPOLOGICAL QUANTUM COMPUTATION

4.1. Universal Quantum Computation

A quantum computer performs arbitrary unitary operations on a set of N qubits that are all initialized in the $|0\rangle$ state and read out in the computational basis at the end of the computation. The unitary operations are implemented by composing them from simpler operations that act only on

single qubits (single-qubit gates) or pairs of qubits (two-qubit gates). A popular (but certainly not unique) set of gates that allows for the implementation of arbitrary unitary evolutions on all N qubits consists of three single-qubit gates and one two-qubit gate:

- Phase gate S : The $S = e^{-i\pi Z/4}$ gate effects a $\pi/2$ rotation of a single qubit about the z axis.
- Hadamard H : The Hadamard transformation, $H = (Z + X)/\sqrt{2}$, exchanges the Pauli Z and X axes of a qubit.
- T gate: The $T = e^{-i\pi Z/8}$ gate effects a $\pi/4$ rotation about the z axis.
- Controlled-not gate (CNOT): The CNOT bit-flips a target qubit if a control qubit is in the state $|1\rangle$, and leaves the target qubit unchanged if the control qubit is in the $|0\rangle$ state.

Although all three single-qubit operations involve commensurate angles, they enable arbitrary rotations on the Bloch sphere. The reason is that a sequence of two $\pi/4$ rotations about the z and x axes, effected by T and HTH , respectively, corresponds to a single rotation about a new axis by an irrational angle. The Clifford gates $\{S, H, \text{CNOT}\}$ map Pauli product operators on the set of qubits to other Pauli product operators. It is for this reason that the phase gate $S = T^2$ was included above, even though it is in principle redundant. According to the Gottesman–Knill theorem (66), quantum circuits involving only Clifford gates in addition to preparation and readout in the computational basis can be efficiently simulated on a classical computer.

Majorana braiding can implement only two gates out of this universal gate set, namely, the phase and Hadamard gates. Performing a phase gate on a tetron qubit would require one to braid Majoranas γ_1 and γ_2 , i.e., $S = B_{12}$. An implementation of the Hadamard gate requires a sequence of three braids, $H = iB_{12}B_{23}B_{12}$. Several schemes have been proposed to implement braiding of Majoranas in quantum wire architectures, including explicitly moving Majoranas in T-junctions (62), time-dependent protocols of Majorana couplings (64), or measurement-based schemes (11). The latter two schemes have been explicitly developed in situations in which the quantum wires are Coulomb blockaded (11, 32). Neither the T nor the CNOT gate can be implemented by braiding. CNOT gates can be implemented using two-qubit parity measurements and an ancilla qubit in addition to single-qubit Clifford gates (67). **Figure 3a** shows the corresponding equivalent circuit involving an ancilla qubit initialized in a $|+\rangle = (|0\rangle + |1\rangle)/\sqrt{2}$ state. The circuit relies on two-qubit parity measurements of control and ancilla qubits ($Z \otimes Z$) as well as ancilla and target qubits ($X \otimes X$). Subsequently, the ancilla is disentangled by reading it out in the computational basis and corrective single-qubit operations on control and target depending on the measurement outcomes. We discuss in Section 4.2 below how to perform the required two-qubit parity measurements within a Majorana platform.

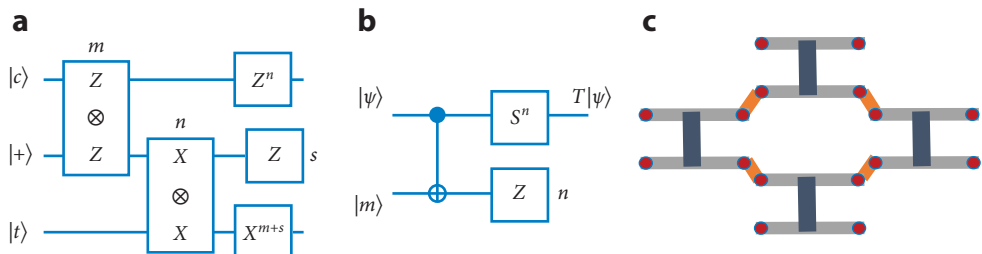


Figure 3

Equivalent circuits for (a) controlled-not gate involving two-qubit parity measurements and (b) implementations of the T -gate with magic states $|m\rangle$. (c) Readout of multiqubit parity.

Several schemes for realizing T gates have been proposed. One option is to rely on magic states (68),

$$|m\rangle = \frac{1}{2}(|0\rangle + e^{i\pi/4}|1\rangle). \quad 14.$$

If magic states exist as a resource, we can implement a T gate on qubits by implementing the equivalent circuit shown in **Figure 3b**. The circuit relies on a CNOT gate applied between the qubit and a magic-state ancilla, followed by disentangling the ancilla by reading it out in the computational basis and a corrective operation depending on the measurement outcome.

Because $|m\rangle = T|+\rangle$, it may seem that preparing magic states already requires one to perform T gates. Indeed, in a first step, one needs to be able to prepare approximate magic states with a certain minimal accuracy, e.g., by implementing T gates in a topologically nonprotected manner. In the simplest case, this could be achieved by inducing a finite energy splitting between the computational states $|0\rangle$ and $|1\rangle$ for an appropriate time interval. These approximate magic states can then be used to produce better magic states by magic-state distillation, a procedure that uses only Clifford gates (68). In practice, many approximate magic states are distilled into a smaller number of better magic states. Multiple rounds of magic-state distillation can be performed until the resulting magic states have the quality required for the actual quantum computation.

An alternative approach to achieve a rather accurate (although not topologically protected) magic gate is based on geometric rather than dynamical phases and was proposed in References 69 and 70. Implementing a phase gate S by adiabatically braiding two Majorana zero modes can be visualized as a path on the Bloch sphere that covers one octant of the entire sphere. This path is associated with the accumulation of a $\pi/4$ Berry phase. The topological protection ensures that the path is followed with exponential accuracy, resulting in a precise S operation. To induce the T gate, one should enclose half of the octant. Generalizing echo and dynamical decoupling methods introduced to improve magnetic resonance measurements, Reference 69 suggests a protocol in which a path covers half an octant by moving back and forth on the Bloch sphere in a judicious manner. As in echo protocols, errors that are accumulated during the forward path tend to cancel on the return. The method was further elaborated and improved in Reference 70 using a combination of projective measurements and nonadiabatic evolution that effectively cancels smooth control errors when implementing phase gates in Majorana-based systems. This scheme can be used either to implement T gates directly or to generate high-quality input states for magic-state distillation. It is also useful for generating rotations by arbitrary angles about the z axis.

4.2. Two-Qubit Parity Measurements

CNOT gates can be performed with Majorana-based topological qubits by exploiting two-qubit parity measurements of $X_i \otimes X_j$ or $Z_i \otimes Z_j$. (Here, the subscripts of the operators enumerate the qubits involved in the measurement.) Furthermore, multiqubit parity measurements are an important ingredient in topological quantum error correction that will be discussed in Section 6. These kinds of operators can in principle be measured by a direct extension of the method used for reading out individual tetron or hexon qubits (see Section 3.3; 10, 11, 65, 71, 72).

Consider the two-qubit parity operator $Z_i \otimes Z_j$ involving qubits encoded in two neighboring hexons as shown in **Figure 2c**. In Majorana representation, this operator is the product of four Majorana operators, two from each hexon. Similar to the readout scheme for individual qubits, gate-controlled semiconductor links introduce hybridizations between Majoranas of the two qubits. This is done in such a way that the shortest nontrivial loop requires electrons to pass through all four Majoranas exactly once. All shorter paths simply retrace themselves, with

Majorana operators appearing twice and squaring to unity. When including quantum dots into the semiconductor links, the self-retracing paths merely shift the energy of the quantum dot levels by a state-independent constant, but the nontrivial loops cause a shift that depends on the two-qubit parity.

This scheme can be generalized in several ways. First, it can be extended to measurements of two-qubit parities with arbitrary Pauli operators. To this end, the semiconductor links are simply implemented between the Majoranas appearing in the Pauli operators.

Second, it can be extended to multiqubit parities (71, 72). As an example, consider a set of four tetrons with Majorana hybridizations as shown in **Figure 3c**. The shortest nontrivial loop involves eight Majoranas, two from each tetron, and thus corresponds to a four-qubit parity such as $Z_1 \otimes Z_2 \otimes Z_3 \otimes Z_4$.

Just as for the qubit readout, these measurements are protected as long as Majorana overlaps within each qubit are exponentially suppressed.

4.3. Tracking Clifford Gates

The operations of a Majorana-based quantum computer can be simplified by exploiting the Gottesman–Knill theorem (66). Instead of explicitly performing Clifford gates, these operations are tracked on a classical computer and subsequent operations are appropriately adapted (11, 65, 73). Tetron- and hexon-based Majorana hardware is well suited for this purpose because it does not prefer one of the three Pauli bases.

The single-qubit Clifford gates S and H rotate the qubit's Pauli basis. The Hadamard gate H maps $Z \rightarrow X$, $X \rightarrow Z$, and $Y \rightarrow -Y$. Similarly, the S gate effects $X \rightarrow Y$, $Y \rightarrow -X$, and $Z \rightarrow Z$. Instead of physically performing these gates by braiding operations, we can adapt later operations to the new Pauli basis, assigning new pairs of Majoranas to the X , Y , and Z operators.

As a simple example, consider a minimal gate circuit involving a single qubit, on which we perform a Hadamard gate H , followed by readout in the computational (Z) basis. Instead of actively implementing the Hadamard gate by braiding, we can equivalently remember that the Hadamard gate exchanges the Pauli X and Z operators and read out the qubit in the X basis without performing the Hadamard transformation. This illustrates that for the purpose of quantum computing applications, the nonabelian statistics of Majoranas is essentially equivalent to the ability to read out Majorana qubits in all three Pauli bases with equal ease and precision.

In addition to single-qubit Clifford gates, it is also possible to track CNOT gates (65). A single CNOT gate transforms $\mathbf{1} \otimes Z \rightarrow Z \otimes Z$, $Z \otimes \mathbf{1} \rightarrow Z \otimes \mathbf{1}$, $\mathbf{1} \otimes X \rightarrow \mathbf{1} \otimes X$, and $X \otimes \mathbf{1} \rightarrow X \otimes X$. Consequently, tracking a Clifford circuit including CNOTs transforms a single-qubit Pauli operator into a nonlocal Pauli product operator such as $X \otimes Y \otimes X \otimes Z \otimes \mathbf{1} \otimes \dots \otimes X$ spanning many qubits. Such operators must then be measured not only during readout but also when implementing T gates using magic states. Instead of entangling qubits using CNOT gates, entanglement is generated through these nonlocal measurements.

Such highly nonlocal operators can be measured using only local two-qubit parity measurements involving neighboring qubits (65). This is based on initializing a GHZ (Greenberger–Horne–Zeilinger) state $|\text{GHZ}\rangle = (|0\rangle^{\otimes n} + |1\rangle^{\otimes n})/\sqrt{2}$ on a set of n ancilla qubits. (This requires initialization of all ancillas in the X basis and subsequent measurements of the two-qubit parities $Z \otimes Z$ between neighboring qubits.) Although the product $\otimes_{j=1}^n X_j = 1$ for a GHZ state, measurements of any individual X_j are completely undetermined. Nonlocal Pauli products on the data qubits can therefore be measured by pairing each data qubit with a neighboring ancilla qubit and measuring $P \otimes X_j$ on these pairs, where P is the Pauli operator involved in the nonlocal Pauli product for this data qubit. Though no information is gained about individual data qubits, the

Pauli product can be extracted from the product of all these measurements. By performing the measurements in parallel, the time required for these procedures is independent of the number of qubits involved in the Pauli product.

5. TOPOLOGICALLY ORDERED SPIN MODELS AND THE SUPERCONDUCTOR–INSULATOR TRANSITION

5.1. Networks of Cooper-Pair Boxes

In Section 3, we introduced tetrons and hexons as realizations of qubits. Protocols for quantum computation largely rely on manipulations by measurement that actively generate entangled quantum states. Alternatively, it is interesting to consider networks of Majorana Cooper-pair boxes that are coupled by hybridizing pairs of Majoranas both within and between boxes.

When the hybridization amplitude t between the boxes is much larger than the charging energy E_C , the system will be in a (possibly topological) superconducting phase, but as E_C/t increases, there will be a transition to an insulator. In the absence of topological superconductivity, this superconductor–insulator transition has been extensively studied for Josephson junction arrays built from Cooper-pair boxes (see Reference 74 for a review).

For Cooper-pair boxes involving topological superconductors, the Majorana zero modes introduce internal degrees of freedom within each Cooper-pair box. This is because tetrons and hexons can alternatively be viewed as spin-1/2 degrees of freedom. Remarkably, this allows for nontrivial insulating phases. Unlike the topological superconducting phase, the insulating phases can be topologically ordered with ground-state degeneracy on a torus and fractionalized excitations having nontrivial commutation relations. Here we review how arrays of Cooper-pair boxes in one, two, or three dimensions can be used to engineer various topologically ordered phases. Interestingly, this is not limited to implementing spin models on the basis of Majorana Cooper-pair boxes. It is also possible (75) to directly implement interesting field theories of interacting bosonic and fermionic fields.

Spin models realized as arrays of tetrons are extensively explored in References 76 and 77, which discuss various representative cases. Here, we emphasize networks of hexons. These are not only more economical as six Majoranas suffice for two spins (instead of eight in the case of tetrons) but also turn out to be more flexible for coupling and tuning the effective spin models. We only consider models that can be engineered through local tunneling and local interactions and which do not require long-range capacitive interactions or tunneling between Majoranas that are not in close spatial proximity. (Models outside this scope were recently reviewed in Reference 19.)

We restrict our analysis to the regime deep in the insulating phase, $t/E_C \ll 1$. In this limit, there is only virtual tunneling between Cooper-pair boxes, and the fluctuations of the phase difference between adjacent superconductors, which drive the superconductor–insulator transition, do not play a significant role.

Although certain insulating phases are equivalent to spin models, there is no general recipe for engineering arbitrary spin models. The physical constraints of local interactions and local tunneling limit the kinds of spin interactions that can be realized.

Several spin models can be solved by introducing Majorana representations for the spins, with Kitaev’s honeycomb model (12) being the most prominent example. The constructions in this section can be viewed as the reverse. We employ the mapping between interacting Majorana zero mode and spin models in order to understand the physics of the resulting insulating phases. Specifically, Majorana Cooper-pair boxes turn out to be particularly convenient for realizing spin models with anisotropic exchange interactions.

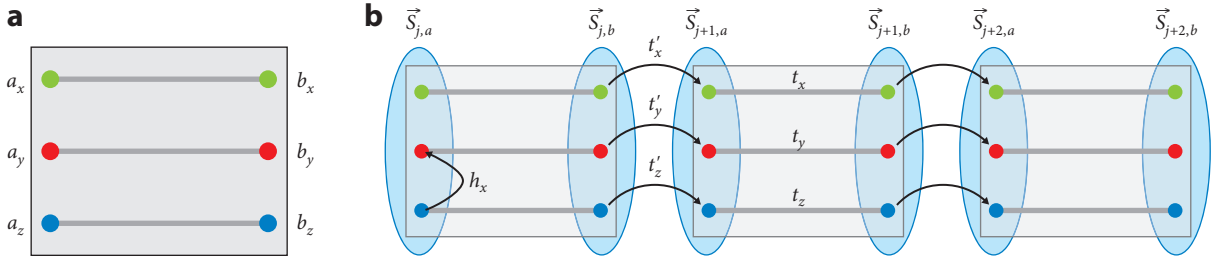


Figure 4

Coupled Majorana Cooper-pair boxes. (a) Basic hexon building block. Its Majorana zero modes represent two spin-1/2 degrees of freedom. (b) Arrays of coupled hexons effectively model spin chains with nontrivial insulating phases. Various insulating phases can be realized by tuning the hybridizations t and b by means of local gate potentials. In addition to spin models, such constructions can also be used to directly implement quantum field theories. Figure adapted from Reference 80.

5.2. Spin Interactions from Hexons

When viewing tetrons and hexons as spin-1/2 degrees of freedom, their spin operator \mathbf{S} is related to the Pauli operators defined in Sections 3.1 and 3.2 in the usual way: $\mathbf{S}^x = X/2$, $\mathbf{S}^y = Y/2$, and $\mathbf{S}^z = Z/2$. The Zeeman field and the interactions between the spins can be tuned by gate potentials controlling the tunneling amplitude between the Majoranas within each Cooper-pair box and between the boxes.

Translating the results of Section 3.2 to spin language, the hybridization t_α of Majoranas a_α and b_α of a single wire (see **Figure 4**) effectively introduces exchange interactions $J_\alpha S_{n,a}^\alpha S_{n,b}^\alpha$ between the two spins encoded by the hexon n . This intrahexon exchange coupling J_α is linear in the hybridization t_α and allows for tuning the sign of J_α . Indeed, the overlap t_α between Majorana zero modes generically changes sign as a function of gate voltage or magnetic field (see Section 2.2).

A different set of terms is generated by coupling Majorana zero modes of the same type (a with a and b with b), e.g., by changing the distance between wires. These terms generate the effective Zeeman coupling,

$$i \sum_{\alpha\alpha'} t_{\alpha\alpha'} (a_\alpha a_{\alpha'} + b_\alpha b_{\alpha'}) = \sum_\alpha B_\alpha (S_a^\alpha + S_b^\alpha), \quad 15.$$

with an effective Zeeman field $B_\alpha \propto \epsilon_{\alpha\beta\gamma} t_{\beta\gamma}$.

Exchange couplings $S_{n,b}^\alpha S_{n',a}^\alpha$ between spins in adjacent boxes n and n' can be generated by connecting different hexons. Tunneling terms of the form $i \sum_{\alpha=x,y,z} t'_{\alpha} \sum_n b_{an} a_{an+1}$ change the fermion parity of the hexons and therefore do not commute with the constraint (11). Under the assumption that the charging energy E_C is the largest energy scale, higher-order processes that preserve the parity generate interaction terms that commute with the constraint. These terms are obtained from a Schrieffer–Wolff transformation (78) and take the form of exchange couplings between spins in neighboring hexons,

$$\sum_{\alpha=x,y,z} J_\alpha \sum_j S_{j,b}^\alpha S_{j+1,a}^\alpha. \quad 16.$$

Here, the exchange coupling $J_\alpha \propto \frac{\prod_{\alpha' \neq \alpha} t'_{\alpha'}}$ is second order in the tunneling amplitudes.

5.3. One-Dimensional Superconductors and Spin Chains

We first consider one spatial dimension. Linear chains of coupled hexons can then implement a variety of interesting spin models.

5.3.1. SU(2)-invariant spin chains. A chain of hexons as depicted in **Figure 4** is equivalent to an array of spins, which we label by $\mathbf{S}_{n,\gamma}$. Here, n enumerates the hexons and $\gamma = a, b$ differentiates between the two spins of each hexon.

When the distance between the wires is large, the Majoranas constituting a particular spin degree of freedom are uncoupled and the effective Zeeman field vanishes. At low energies, neighboring spins of the hexon chain are exchange coupled, both within hexons with strength J_α and between hexons with strength J'_α . The model becomes SU(2) invariant when tuning the exchange couplings such that $J_\alpha = J$ and $J'_\alpha = J'$.

For antiferromagnetic couplings $J, J' > 0$, the model has two distinct dimerized phases. When $J > J'$, we obtain a fully gapped dimerized phase in which the pair of spins in each hexon forms a singlet state. In the opposite regime $J' > J$, the spin chain is again in a gapped dimerized phase, now with adjacent spins from neighboring hexons forming singlet states (79). These two phases are topologically distinct, with the second state supporting protected boundary spins at the two ends of a finite chain. The critical point separating these phases occurs at $J = J'$, where the model becomes the spin-1/2 Heisenberg model. The latter is known to be dual to a gapless Luttinger liquid model of interacting fermions.

Given that the charge degrees of freedom of the hexon chain are gapped, electronic transport measurements do not provide experimental signatures of the intervening phase transition. An alternative route relies on thermal conductance measurements. Although such measurements are possible, they are typically difficult in practice. Reference 80 discusses how the critical state is reflected in correlations between the effective spins that can be extracted experimentally from charge polarization measurements.

5.3.2. Transverse field Ising model. The transverse field Ising model is constructed by implementing anisotropic exchange couplings with $J_z = J'_z = J$ and $J_x = J_y = J'_x = J'_y = 0$, both within and between the hexons of the chain. Relative to the SU(2)-invariant case, this is done by only turning on the couplings between a_z^n and b_z^n within each hexon and only turning them off between the hexons.¹ To generate the transverse field, the b_x couplings between the Majoranas representing a single spin are turned on. Varying J or b_x , the system can be tuned through an Ising phase transition with central charge $c = 1/2$. Its critical exponents can be extracted from charge polarization measurements. A phase transition in the same universality class can be realized by tuning the couplings between the Majoranas such that there is J_x exchange coupling between the spins within a hexon and J'_y coupling between spins of neighboring hexons.

5.3.3. Supersymmetric tricritical Ising theory. A one-dimensional tricritical Ising model is interesting from a theoretical point of view as the properties of its tricritical point are described by a minimal supersymmetric conformal field theory with central charge $c = 7/10$. As such, it may open a route toward universal topological quantum computation. Indeed, in two spatial dimensions a model that is gapped in the bulk but supports a chiral boundary mode with central charge

¹Notice that $J'_x = J'_y = 0$, and $J'_z \neq 0$ can be implemented, but in general, the three couplings are not independent owing to the cyclic relation $J'_x \propto t'_y t'_z / E_C$, $J'_y \propto t'_x t'_z / E_C$, and $J'_z \propto t'_x t'_y / E_C$ so that not all spin models are easily realized.

$c = 7/10$ carries Fibonacci particles. Their braiding statistics allow for the implementation of a computationally complete set of quantum gate operations and thus universal topological quantum computation (24).

5.3.3.1. Blume–Capel model. This tricritical Ising transition is realized in the spin-1 Blume–Capel model,

$$H_{\text{BC}} = \sum_j \alpha \mathbf{S}_x^j + \delta (\mathbf{S}_z^j)^2 - J \mathbf{S}_z^j \mathbf{S}_z^{j+1}. \quad 17.$$

Notice that here, the $\mathbf{S}_{z,(x)}^j$ are spin-1 operators along the z (x) axis at site j . It is known from numerical studies that in this model, the tricritical point occurs for $\alpha \sim \delta$ (81). Reference 75 shows how to tune the couplings between the Majorana zero modes such that effective α and δ couplings are obtained and can be tuned to the tricritical point. In this construction, the effective spin-1 degrees of freedom are obtained by tuning $t_x = t_y = t_z$ such that a strong ferromagnetic coupling is obtained between the two spin-1/2s within each hexon.

5.3.3.2. Supersymmetric field theory. The tricritical Ising transition is also analytically known to be described by a supersymmetric field theory with one bosonic and one real fermionic field (81). This field theory can be implemented directly in a system of three coupled Majorana chains, circumventing a mapping to spins. Two chains are effectively used to realize a bosonic field (by bosonization of the complex fermionic field), and the remaining chain realizes the real fermion. Reference 75 shows how to tune the t and h of **Figure 4** as well as the charging energy E_C to realize the couplings of the field theory. This implementation relies on treating the (large) charging energy using a Villain transformation and the resulting sine-Gordon-like terms in a mean-field approximation.

5.4. Kitaev Honeycomb Model and Yao–Kivelson Model in Two Dimensions

These examples illustrate that hexons are fruitful building blocks for realizing one-dimensional spin chains. Reference 80 extends these ideas to two dimensions by constructing the Yao–Kivelson model (82). This model realizes a topologically ordered state that is dual to the nonabelian Kitaev spin-liquid state.

The underlying arrangement of the hexon network is shown in **Figure 5a,b**. Notice that the labels x , y , and z of the Majorana zero modes are alternating between hexons. In each hexon, the Majoranas at the ends of the colored wire are hybridized, which induces exchange couplings $S_a^\alpha S_b^\alpha$. In addition, loop tunneling terms straddling neighboring hexons generate $S_a^\alpha S_b^\alpha$ -type terms, with α determined by geometry as illustrated in **Figure 5a**. The inset of **Figure 5a** summarizes the resulting dominant spin interactions. It is worthwhile to emphasize that it is the use of the hexon building blocks that allows one to implement all interactions by local couplings between the Majoranas only.

Connecting many such building blocks in a decorated honeycomb lattice geometry implements the Yao–Kivelson Hamiltonian. This model is known to exhibit a nonabelian spin-liquid state equivalent to the B-phase of the Kitaev honeycomb model (12). Unlike in the Kitaev case, the Yao–Kivelson model breaks time reversal symmetry spontaneously. The abelian A-phase of the Kitaev honeycomb model (represented by the toric code) can also be realized by making one type of the intrahexon exchange couplings much larger than the other two. More direct implementations of the toric code based on tetrons were presented in References 72 and 83, but these are restricted to the A-phase only.

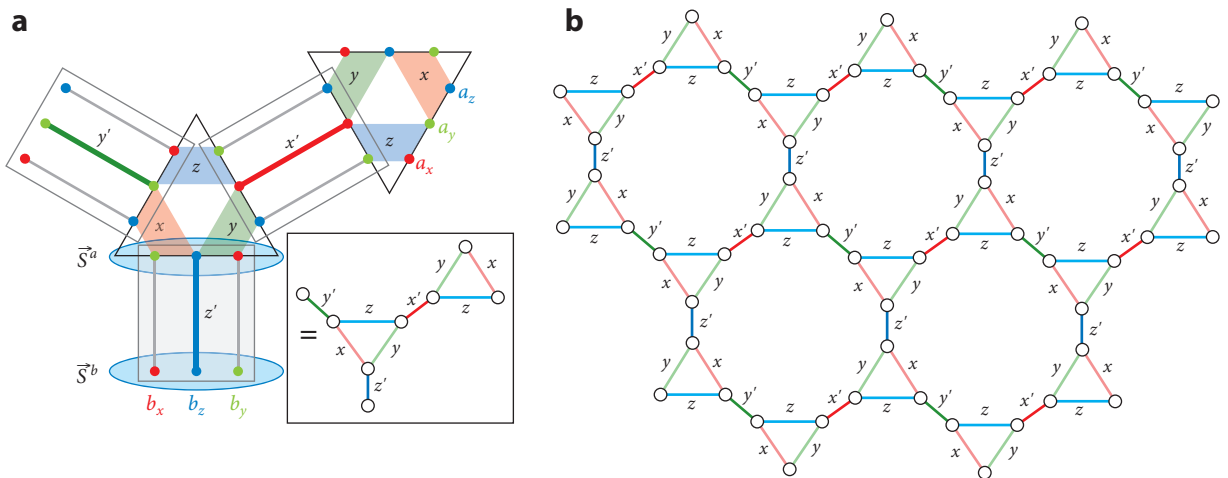


Figure 5

Hexon construction for the Yao–Kivelson model. (a) Coupling of the basic hexon building blocks. (b) Two-dimensional spin network resulting from the coupled hexon array. Colors and labels of the bonds indicate the direction of the exchange coupling. Figure adapted from Reference 80.

5.5. String-Net Models and Fracton Codes

Majorana Cooper-pair boxes have also been proposed as building blocks to engineer more involved topological phases. These efforts are driven by the quest to engineer phases with computationally more powerful anyons and the lack of realistic systems that are described by some of these intriguing Hamiltonians. Reference 84 describes a Majorana-based implementation of the double semion model as the simplest string net model beyond the toric code.

Majorana Cooper-pair boxes can in principle also be used to engineer a variety of fracton phases in three-dimensional spin models (85). Although fracton models usually involve complicated spin-cluster interactions, these can be obtained from potentially more physical Majorana models in the limit of strong local interactions (85, 86).

6. TOPOLOGICAL QUANTUM ERROR CORRECTION IN MAJORANA-BASED ARCHITECTURES

6.1. Surface and Color Codes

Section 4 sketched a Majorana-based scheme for universal quantum computation. Within this scheme, the length of quantum computations will be limited to the lifetime of the individual physical qubits. Although Majorana-based topological qubits may have a long lifetime (1, 87–90), this may not suffice for some quantum computations. Majorana-based topological hardware would then need to be combined with quantum error correction (16). The potential advantage of topological qubits over nontopological qubits would be their lower error rate. This may substantially reduce the number of physical qubits required for the logical qubits underlying the quantum error correction.

An important topological error correcting code with a high error threshold is the surface code (91–93). The quantum information is stored in a square array of physical qubits, with the logical subspace defined by fixing a set of stabilizer (generator) operators to unity. There is one stabilizer

operator per plaquette of the lattice, alternating between $X_1 \otimes X_2 \otimes X_3 \otimes X_4$ and $Z_1 \otimes Z_2 \otimes Z_3 \otimes Z_4$ in a checkerboard fashion. Each stabilizer involves the four qubits adjacent to the plaquette, has eigenvalues equal to ± 1 , and commutes with all other stabilizers.

When defined on a torus (toric code; 91, 94), the resulting state is fourfold degenerate, reflecting its Z_2 topological order. Logical qubit operators distinguish between the states in this manifold and commute with all stabilizers. In keeping with the fourfold degeneracy, there are two sets of logical Pauli operators. These take the form of string operators involving products of Pauli operators around the two nontrivial loops of the torus. In a planar arrangement (surface code), logical subspaces can be defined by “punching holes” in the surface code (95), i.e., by not measuring certain stabilizers, or by appropriate boundary stabilizers of finite surface code patches (92).

Quantum information can be stored fault-tolerantly in these logical subspaces. Errors are detected by stroboscopic measurements of all stabilizers. For a sufficiently small error rate, errors can be actively corrected (or simply tracked, appropriately adapting subsequent measurements) without compromising the encoded quantum information (91, 93).

For many physical implementations of qubits, the stabilizer operators involving four spin operators are difficult to measure directly, and one must resort to a quantum circuit involving an additional ancilla qubit for every plaquette (95). This circuit involves four CNOT gates with the plaquette qubits as controls and the ancilla as the target qubit, and a final readout measurement of the ancilla.

A tetron-based Majorana hardware has the advantage that the stabilizer operators can be measured directly (65, 71, 72, 83). As reviewed in Section 4.2, this is achieved by employing closed tunneling paths connecting the four qubits of a plaquette. Each Pauli operator is a product of two Majoranas, and the plaquette operators involve the eight Majoranas adjacent to the plaquette.

It is in general nontrivial to perform quantum gates on logical qubits (93, 95). In particular, there is frequently no relation between performing a quantum gate on the physical qubits and performing the same quantum gate on the level of the logical qubit. Exceptions are referred to as transversal gates. These gates can be performed at the level of the logical qubit by performing the gate in parallel on all its physical qubits.

In the context of Majorana quantum computation, planar color codes have particularly interesting transversal gates (96). Their transversal gates are just the Clifford gates (97, 98), including the single-qubit Clifford gates that can be implemented by Majorana braiding. Logical qubits based on planar color codes would therefore be compatible with implementing single-qubit Clifford gates by Majorana braiding and therefore benefit from the corresponding topological protection. A corresponding Majorana architecture was proposed in Reference 96.

At the same time, color codes require stabilizer measurements involving six-qubit operators, as opposed to the four-qubit stabilizers of surface codes. Below, we review how quantum gates can be performed for surface code patches in a closely analogous manner to the scheme for physical tetron and hexon qubits in Section 4 above. In particular, this scheme is compatible with tracking all Clifford gates (65, 99).

6.2. Majorana Surface Codes

Surface codes can be viewed as lattice models with qubits placed at the vertices of a square lattice and stabilizer operators associated with every lattice plaquette. Then, the logical subspace is the ground-state manifold of the Hamiltonian

$$H = - \sum_{\text{light}} X_{p1} X_{p2} X_{p3} X_{p4} - \sum_{\text{dark}} Z_{p1} Z_{p2} Z_{p3} Z_{p4}, \quad 18.$$

which is a sum over the mutually commuting stabilizer operators. It is important to understand, however, that active error correction relies on performing stroboscopic stabilizer measurements on otherwise uncoupled qubits instead of implementing stabilizers as Hamiltonian terms!

When implementing the qubits as tetrons, the plaquette operators can be written as products over all Majoranas around the plaquette, independent of whether the operator is associated with a light or a dark plaquette (72, 83). Furthermore, the implementation of the qubit by a tetron relies itself on a parity constraint that involves the product over all of its four Majoranas. This implies that we can alternatively interpret the surface code as a Majorana fermion code (100) in which the commuting stabilizers involve all Majorana operators around the lattice plaquettes. To do so, we split each vertex of the surface code lattice into four vertices, which host the Majoranas associated with the tetron. The resulting tiling is illustrated in **Figure 6**.

Such Majorana fermion codes can be defined for tilings for which adjacent plaquettes share an even number of vertices (100). In view of the anticommutation relations of Majoranas, this ensures that the plaquette operators commute with one another. The surface code on a square lattice corresponds to a 4.8.8 tiling, reflecting the number of sites of the plaquettes meeting at any vertex.

There are two additional uniform tilings that support a Majorana fermion code (see **Figure 6**). One such tiling is the honeycomb lattice (71). The corresponding 6.6.6 Majorana surface code places Majoranas at the vertices of the honeycomb lattice. The stabilizer operators now involve only six Majoranas, which is less than required for implementing the 4.8.8 code. This may be advantageous if stabilizer measurements turn out to be challenging. Similar to the 4.8.8 code, a physical implementation would rely on Coulomb-blockaded islands hosting six Majoranas each for, say, the green plaquettes, and implementing the remaining stabilizers as measurements performed by defining appropriate loops.

The third tiling derives from the toric code with qubits placed on the vertices of a Kagome lattice (or, equivalently, the bonds of a honeycomb lattice) and replacing all qubits by tetrons. This results in a 4.6.12 Majorana surface code (65). Additional Majorana fermion codes can be generated based on nonuniform tilings (100) or on concatenation of codes (65, 100).

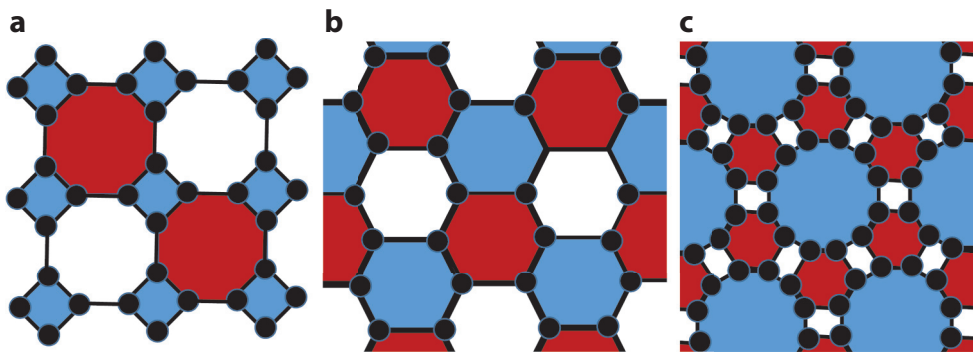


Figure 6

Majorana surface codes based on uniform tilings. (a) 4.8.8 code with Majoranas located at all vertices. Stabilizers are associated with the product of Majoranas around each plaquette. When implementing blue stabilizers as parity constraints of Coulomb-blockaded islands, this is just a bosonic surface code with tetron qubits. (b) 6.6.6 code. (c) 4.6.12 code. Implementations would realize one type of plaquette as Majorana Cooper-pair boxes and the remaining stabilizers by measurement. Figure adapted from Reference 65.

6.3. Applications to Quantum Computing

The long coherence times of Majorana-based qubits may make it sufficient to rely on small Majorana-based error correcting codes (101). Alternatively, Majorana surface codes provide a highly flexible platform for which the code distance (i.e., the level of topological protection provided by the error correcting code) can be flexibly adapted to the underlying hardware. Majorana surface codes exist with arbitrary code distance. The various codes differ in the number of physical qubits required for a logical qubit of a given code distance as well as in the number of Majoranas involved in a stabilizer measurement (65). A denser encoding requiring fewer Majoranas for a given code distance typically comes with a larger number of Majoranas involved in a stabilizer measurement. The optimal trade-off would ultimately depend on hardware specifics.

Universal quantum computation can be implemented for all Majorana surface codes using the same basic scheme (65). This scheme is closely analogous to the one for tetron and hexon qubits discussed in Section 4. In fact, tetrans and hexons can be viewed as Majorana surface code patches with the smallest code distance. Furthermore, surface code patches share important properties with tetrans and hexons (65). The Pauli X and Z operators of a tetron are associated with the two Majoranas along the horizontal and vertical edges, respectively. Similarly, the logical X and Z operators of surface code patches are associated with its horizontal and vertical edges, and involve a product over the X and Z operators of all physical qubits along these edges. In this sense, surface code patches effectively behave as logical tetrans.

In these logical tetrans, horizontal and vertical edges are distinguished by whether the two-qubit boundary stabilizers involve Pauli Z or X operators. By switching the boundary stabilizers along the same edge, one can define surface code patches that are closely analogous to hexons and encode two logical qubits (65, 99).

Logical hexons encode qubits for which the logical X and Z operators are both located on the same side of the surface code patch. Just as for physical hexons, this provides the flexibility for tracking Clifford gates (65). As we saw above, an essential requirement is the ability to measure arbitrary two-qubit parities. This can be achieved for surface code patches by lattice surgery, which introduces new boundary stabilizers that straddle the boundaries of the two participating qubits (102). The two-qubit parity can then be extracted as a product of these boundary stabilizers.

The measurement of arbitrary combinations of Pauli operators can be implemented using twist-based lattice surgery. In this scheme, the chain of interqubit stabilizers involves twist defects of the surface code lattice (99). Such lattice surgery protocols can be defined for any of the Majorana surface codes as well as Majorana color codes resulting from concatenating Majorana surface codes with small Majorana codes. Thus, all these platforms for fault-tolerant quantum computation are compatible with tracking all Clifford gates (65).

7. CONCLUSIONS AND FUTURE PERSPECTIVES

Majorana zero modes have captured the imagination of condensed matter physicists because of their remarkable properties and their potential use in topological quantum computation. This review focused on recent advances that demonstrate that Coulomb charging effects provide a remarkably rich and promising addition to Majorana physics.

In the context of topological quantum computation, Coulomb charging can be exploited for suppressing quasiparticle poisoning processes in topological qubits; for performing measurements for qubit readout, initialization, or manipulation; and for implementing topological quantum error correction in a Majorana-based hardware. The basic building blocks in these developments are Majorana Cooper-pair boxes, also referred to as tetrans and hexons, which act as topological qubits.

In a closely related development, networks of coupled Majorana Cooper-pair boxes have been proposed as platforms to engineer topologically ordered phases. Charging effects introduce interactions among the Majoranas, which drive the underlying topological superconductors into non-trivial insulating states. Examples of this have been proposed in one, two, and three dimensions.

Current experimental techniques using proximity-coupled semiconductor quantum wires or two-dimensional electron systems as well as selective area growth already seem well adapted for implementing such networks in one and two dimensions. As such networks come within experimental reach, it will be increasingly interesting to study them for broader parameter ranges, exploring their phase diagrams and their quantum phase transitions beyond the limit of strong interactions that dominated much of the work done so far. Reducing the charging energy leads to larger energy scales of the interaction between the spins and, thus, potentially larger gaps, but it also introduces more involved spin interactions or even invalidates the mapping to spins entirely.

It will also be important to study the effects of disorder in both the couplings and the charging energies on the system properties. Although these may be detrimental, the topologically ordered phases should exhibit some level of resilience against disorder by virtue of their excitation gap. In principle, it is even conceivable that interesting topologically ordered phases can be supported by appropriate granular superconductors.

Similarly, the success of Coulomb-charging-based protocols for Majorana-based quantum computation will in practice also depend on various more microscopic aspects of these systems. One of the important questions in this context is the accuracy and the timescales of measurements on topological qubits.

It is clear that there are still numerous possible extensions such as larger numbers of Majoranas in a single Coulomb-blockaded island. Perhaps, it is possible to use some of these extensions to realize topologically ordered phases that support a computationally complete set of nonabelian anyons. For instance, the extension of the supersymmetric model discussed in Section 5.3.3 to $2 + 1$ dimensions would support Fibonacci particles. Even though Majorana-based quantum computation can be made universal, e.g., using magic-state distillation, it would be extremely interesting to realize these phases.

DISCLOSURE STATEMENT

The authors are not aware of any affiliations, memberships, funding, or financial holdings that might be perceived as affecting the objectivity of this review.

ACKNOWLEDGMENTS

We are indebted to our collaborators who contributed to works related to the topic of this review, including Jason Alicea, Bela Bauer, Erez Berg, Parsa Bonderson, Piet Brouwer, Hiromi Ebisu, Jens Eisert, Matthew Fisher, Karsten Flensberg, Michael Freedman, Leonid Glazman, Arbel Haim, Bert Halperin, Matthew Hastings, Torsten Karzig, Markus Kesselring, Thomas Kiendl, Christina Knapp, Daniel Litinski, Roman Lutchyn, Charlie Marcus, Ryan Mishmash, Chetan Nayak, Yang Peng, Falko Pientka, Stephan Plugge, Gil Refael, Eran Sagi, Eran Sela, Ady Stern, Yukio Tanaka, and Yizhi You. We also acknowledge support by the European Union's Horizon 2020 research and innovation program under the LEGOTOP grant agreement No. 788715, the DFG (CRC/Transregio 183 and CRC 910), QuantERA (TOPOQUANT), the Israel Science Foundation, and the Binational Science Foundation.

LITERATURE CITED

1. Kitaev AY. 2003. *Ann. Phys.* 303:2–30
2. Moore G, Read N. 1991. *Nucl. Phys. B* 360:362–96
3. Nayak C, Wilczek F. 1996. *Nucl. Phys. B* 479:529–53
4. Ivanov DA. 2001. *Phys. Rev. Lett.* 86:268–71
5. Stern A, von Oppen F, Mariani E. 2004. *Phys. Rev. B* 70:205338
6. Kitaev AY. 2001. *Phys. Uspekhi* 44:131
7. Fu L. 2010. *Phys. Rev. Lett.* 104:056402
8. Lutchyn RM, Sau JD, Das Sarma S. 2010. *Phys. Rev. Lett.* 105:077001
9. Oreg Y, Refael G, von Oppen F. 2010. *Phys. Rev. Lett.* 105:177002
10. Plugge S, Rasmussen A, Egger R, Flensberg K. 2017. *New J. Phys.* 19:012001
11. Karzig T, Knapp C, Lutchyn RM, Bonderson P, Hastings MB, et al. 2017. *Phys. Rev. B* 95:235305
12. Kitaev AY. 2006. *Ann. Phys.* 321:2–111
13. Balents L, Fisher MPA, Nayak C. 1999. *Phys. Rev. B* 60:1654–67
14. Senthil T, Fisher MPA. 2000. *Phys. Rev. B* 62:7850–81
15. Wang C, Potter AC, Senthil T. 2013. *Phys. Rev. B* 88:115137
16. Terhal BM. 2015. *Rev. Mod. Phys.* 87:307–46
17. Krogstrup P, Ziino NLB, Chang W, Albrecht SM, Madsen MH, et al. 2015. *Nat. Mat.* 14:400–6
18. Albrecht S, Higginbotham A, Madsen M, Kuemmeth F, Jespersen T, et al. 2016. *Nature* 531:206–9
19. Rahmani A, Franz M. 2019. *Rep. Prog. Phys.* 82:084501
20. Gangadharaiah S, Braunecker B, Simon P, Loss D. 2011. *Phys. Rev. Lett.* 107:036801
21. Sela E, Altland A, Rosch A. 2011. *Phys. Rev. B* 84:085114
22. Stoudenmire EM, Alicea J, Starykh OA, Fisher MP. 2011. *Phys. Rev. B* 84:014503
23. Béri B, Cooper NR. 2012. *Phys. Rev. Lett.* 109:156803
24. Nayak C, Simon S, Stern A, Freedman M, Sarma S. 2008. *Rev. Mod. Phys.* 80:1083–159
25. Alicea J. 2012. *Rep. Prog. Phys.* 75:076501
26. Beenakker CWJ. 2013. *Annu. Rev. Condens. Matter Phys.* 4:113–36
27. Aguado R. 2017. *Riv. Nuovo Cimento* 40:523–93
28. von Oppen F, Peng Y, Pientka F. 2017. In *Topological Aspects of Condensed Matter Physics*, ed. C Chamon, M Goerbig, R Moessner, L Cugliandolo, pp. 387–449. Oxford, UK: Oxford Univ. Press
29. Lutchyn R, Bakkers E, Kouwenhoven L, Krogstrup P, Marcus C, Oreg Y. 2018. *Nat. Rev. Mat.* 3:52–68
30. Haim A, Oreg Y. 2019. *Phys. Rep.* 825:1–48
31. van Heck B, Akhmerov AR, Hassler F, Burrello M, Beenakker CWJ. 2012. *New J. Phys.* 14:035019
32. Aasen D, Hell M, Mishmash RV, Higginbotham A, Danon J, et al. 2016. *Phys. Rev. X* 6:031016
33. Mourik V, Zuo K, Frolov S, Plissard S, Bakkers E, Kouwenhoven L. 2012. *Science* 336:1003–7
34. Das A, Ronen Y, Most Y, Oreg Y, Heiblum M, Shtrikman H. 2012. *Nat. Phys.* 8:887–95
35. Churchill HOH, Fatemi V, Grove-Rasmussen K, Deng MT, Caroff P, et al. 2013. *Phys. Rev. B* 87:241401
36. Deng S, Viola L, Ortiz G. 2012. *Phys. Rev. Lett.* 108:036803
37. Law KT, Lee PA, Ng TK. 2009. *Phys. Rev. Lett.* 103:237001
38. Flensberg K. 2010. *Phys. Rev. B* 82:180516
39. Zhang H, Liu CX, Gazibegovic S, Xu D, Logan JA, et al. 2018. *Nature* 556:74–79
40. Nichele F, Drachmann ACC, Whiticar AM, O’Farrell ECT, Suominen HJ, et al. 2017. *Phys. Rev. Lett.* 119:136803
41. Vaitiekėnas S, Deng M-T, Krogstrup P, Marcus CM. 2018. arXiv:1809.05513
42. Lutchyn RM, Winkler GW, van Heck B, Karzig T, Flensberg K, et al. 2018. arXiv:1809.05512
43. Pientka F, Keselman A, Berg E, Yacoby A, Stern A, Halperin BL. 2017. *Phys. Rev. X* 7:021032
44. Fornieri A, Whiticar AM, Setiawan F, Portolés Marín E, Drachmann ACC, et al. 2019. *Nature* 569:89–92
45. Ren H, Pientka F, Hart S, Pierce A, Kosowsky M, et al. 2019. *Nature* 569:93–98
46. Nadj-Perge S, Drozdov IK, Li J, Chen H, Jeon S, et al. 2014. *Science* 346:602–7
47. Ruby M, Pientka F, Peng Y, von Oppen F, Heinrich BW, Franke KJ. 2015. *Phys. Rev. Lett.* 115:197204
48. Pawlak R, Kisiel M, Klinovaja J, Meier T, Kawai S, et al. 2016. *NPJ Quant. Inf.* 2:16035

49. Feldman BE, Randeria MT, Li J, Jeon S, Xie Y, et al. 2017. *Nat. Phys.* 13:286–91
50. Kim H, Palacio-Morales A, Posske T, Rózsa L, Palotás K, et al. 2018. *Sci. Adv.* 4:eaar5251
51. Shabani J, Kjaergaard M, Suominen HJ, Kim Y, Nichele F, et al. 2016. *Phys. Rev. B* 93:155402
52. Chang W, Albrecht SM, Jespersen TS, Kuemmeth F, Krogstrup P, et al. 2015. *Nat. Nanotech.* 10:232–36
53. Reeg C, Loss D, Klinovaja J. 2017. *Phys. Rev. B* 96:125426
54. Reeg C, Loss D, Klinovaja J. 2018. *Phys. Rev. B* 97:165425
55. Winkler GW, Antipov AE, van Heck B, Soluyanov AA, Glazman LI, et al. 2019. *Phys. Rev. B* 99:245408
56. Kiendl T, von Oppen F, Brouwer PW. 2019. *Phys. Rev. B* 100:035426
57. van Heck B, Lutchyn RM, Glazman LI. 2016. *Phys. Rev. B* 93:235431
58. Drukier C, Zirnstein HG, Rosenow B, Stern A, Oreg Y. 2018. *Phys. Rev. B* 98:161401
59. Whiticar AM, Fornieri A, O’Farrell ECT, Drachmann ACC, Wang T, et al. 2019. arXiv:1902.07085
60. Albrecht SM, Hansen EB, Higginbotham AP, Kuemmeth F, Jespersen TS, et al. 2017. *Phys. Rev. Lett.* 118:137701
61. Galindo A, Pascual P. 1990. *Quantum Mechanics I*. Berlin/New York: Springer-Verlag
62. Alicea J, Oreg Y, Refael G, von Oppen F, Fisher MP. 2011. *Nat. Phys.* 7:412–17
63. Halperin B, Oreg Y, Stern A, Refael G, Alicea J, von Oppen F. 2012. *Phys. Rev. B* 85:144501
64. Sau JD, Clarke DJ, Tewari S. 2011. *Phys. Rev. B* 84:094505
65. Litinski D, von Oppen F. 2018. *Phys. Rev. B* 97:205404
66. Gottesman D. 1999. In *Proceedings of the XXII International Colloquium on Group Theoretical Methods in Physics*, ed. SP Corney, R Delbourgo, PD Jarvis, pp. 32–43. Cambridge, MA: International
67. Zilberberg O, Braunecker B, Loss D. 2008. *Phys. Rev. A* 77:012327
68. Bravyi S, Kitaev A. 2005. *Phys. Rev. A* 71:022316
69. Karzig T, Oreg Y, Refael G, Freedman MH. 2016. *Phys. Rev. X* 6:031019
70. Karzig T, Oreg Y, Refael G, Freedman MH. 2019. *Phys. Rev. B* 99:144521
71. Vijay S, Hsieh TH, Fu L. 2015. *Phys. Rev. X* 5:041038
72. Landau L, Plugge S, Sela E, Altland A, Albrecht S, Egger R. 2016. *Phys. Rev. Lett.* 116:050501
73. Litinski D, von Oppen F. 2017. *Phys. Rev. B* 96:205413
74. Schön G, Zaikin AD. 1990. *Phys. Rep.* 98:237–412
75. Ebisu H, Sagi E, Oreg Y. 2019. *Phys. Rev. Lett.* 123:026401
76. Barkeshli M, Sau JD. 2015. arXiv:1509.07135
77. Thomson A, Pientka F. 2018. arXiv:1807.09291
78. Schrieffer JR, Wolff PA. 1966. *Phys. Rev.* 149:491–92
79. Auerbach A. 1994. *Interacting Electrons and Quantum Magnetism*. New York: Springer-Verlag
80. Sagi E, Ebisu H, Tanaka Y, Stern A, Oreg Y. 2019. *Phys. Rev. B* 99:075107
81. Mussardo G. 2017. *Statistical Field Theory: An Introduction to Exactly Solved Models in Statistical Physics*. Oxford, UK: Oxford Univ. Press
82. Yao H, Kivelson SA. 2007. *Phys. Rev. Lett.* 99:247203
83. Plugge S, Landau LA, Sela E, Altland A, Flensberg K, Egger R. 2016. *Phys. Rev. B* 94:174514
84. Wille C, Egger R, Eisert J, Altland A. 2019. *Phys. Rev. B* 99:115117
85. You Y, von Oppen F. 2019. *Phys. Rev. Research* 1:013011
86. You Y, Litinski D, von Oppen F. 2019. *Phys. Rev. B* 100:054513
87. Goldstein G, Chamon C. 2011. *Phys. Rev. B* 84:205109
88. Rainis D, Loss D. 2012. *Phys. Rev. B* 85:174533
89. Knapp C, Karzig T, Lutchyn RM, Nayak C. 2018. *Phys. Rev. B* 97:125404
90. Lai HL, Yang PY, Huang YW, Zhang WM. 2018. *Phys. Rev. B* 97:054508
91. Kitaev AY. 1997. In *Quantum Communication, Computing, and Measurement*, ed. O Hirota, AS Holevo, CM Caves, pp. 181–88. New York: Springer Sci. Bus. Media
92. Bravyi SB, Kitaev AY. 1998. arXiv:9811052
93. Dennis E, Kitaev A, Landahl A, Preskill J. 2002. *J. Math. Phys.* 43:4452–505
94. Wen XG. 2003. *Phys. Rev. Lett.* 90:016803
95. Fowler AG, Mariantoni M, Martinis JM, Cleland AN. 2012. *Phys. Rev. A* 86:032324
96. Litinski D, Kesselring MS, Eisert J, von Oppen F. 2017. *Phys. Rev. X* 7:031048

97. Bombin H, Martin-Delgado MA. 2006. *Phys. Rev. Lett.* 97:180501
98. Landahl AJ, Anderson JT, Rice PR. 2011. arXiv:1108.5738
99. Litinski D, von Oppen F. 2018. *Quantum* 2:62
100. Bravyi S, Terhal BM, Leemhuis B. 2010. *New J. Phys.* 12:083039
101. Hastings MB. 2017. *Quantum Inf. Comput.* 17:1191–205
102. Horsman C, Fowler AG, Devitt S, Meter RV. 2012. *New J. Phys.* 14:123011